Temporal characteristics of resonant surface polaritons in superlensing planar double-negative slabs: Development of analytical schemes and numerical models

Dimitrios L. Sounas, Nikolaos V. Kantartzis, and Theodoros D. Tsiboukis*
Department of Electrical and Computer Engineering, Aristotle University of Thessaloniki, Thessaloniki GR-54124, Greece
(Received 25 July 2007; published 17 October 2007)

The temporal behavior of electric fields in arbitrary double-negative planar slabs is systematically investigated in this paper, from both analytical and numerical perspectives. Concerning infinite slabs, a set of exact expressions for an exponential current excitation is derived through an efficient complex analysis, and an integrated study of surface polariton frequencies is performed. Subsequently, the significant case of a source with a random spatial profile is explored in order to obtain rigorous relations for the field and transient phenomena damping time with respect to problem parameters. On the other hand, a robust finite-difference time-domain methodology is introduced for the comprehensive examination of finite slabs, whose numerical simulations dictate the adoption of a resonatorlike discipline. This inevitable, yet very instructive, convention is physically justified by the almost perfect surface mode reflections at the edges of the slab. In this manner, the proposed formulation reveals a prominent increase in the excited polariton amplitude, relative to the corresponding infinite arrangements, which leads to larger transient times.

DOI: 10.1103/PhysRevE.76.046606 PACS number(s): 41.20.Jb, 78.20.Ci, 73.20.Mf, 42.50.Md

I. INTRODUCTION

Double-negative (DNG) or left-handed metamaterials, as Veselago [1] initially named them, are nonphysical composite substances with negative constitutive parameters, typically synthesized using periodic arrays of small metallic structures (thin wires, split-ring resonators) [2–7] or suitably interconnected lumped circuit elements (capacitors, inductors) [8–10]. Since the first actual fabrication in the microwave regime [11], their wide applicability has become an issue of constant scientific research [12–25], especially in the areas of waveguides and radiating devices [26–34]. However, recent studies unveiled the possibility of employing these intriguing media at optical frequencies [35] as well, therefore approaching the concept of perfectly flat lenses along with its practical implementation.

The potential for perfect focusing of electromagnetic waves via planar DNG slabs stems from Pendry's theoretical work [36], which states that such structures, in their infinite rendition, can amplify evanescent waves and reconstruct the subwavelength information of a nearby electromagnetic source in the image plane. This important phenomenon, usually referred to as the superlensing effect, allows the surpassing of the diffraction limit, always present in conventional lens systems. In fact, the preceding amplification of evanescent waves has been attributed to the evolution of specific resonant modes, designated surface polaritons, at the air-metamaterial interfaces, whose properties have been elaborately demonstrated in Refs. [37–40]. Moreover, the role of losses and refractive index deviations from the ideal −1 case has been the subject of several works [41–43], which revealed a general degradation of image quality. In this context, Ref. [44] examined how the length of finite slabs affects the overall focusing behavior, while Refs. [45,46] tackled the difficulties encountered in the finite-difference time-domain (FDTD) implementation of DNG materials, offering useful guidelines for acquiring accurate and reliable results.

Despite the fact that in superlensing systems we are strongly interested in the field amplitude at a specific frequency, the presence of resonance processes, such as the aforementioned surface polaritons, may induce substantial transient phenomena. In this direction, Ref. [47] explores temporal field features through a mechanical analog for the excited modes, whereas in Ref. [16] a FDTD algorithm is incorporated to certify that the amplitude of the reconstructed image undergoes significant fluctuations until it reaches the desired steady state. Furthermore, a thorough parametric study of transient mechanisms in infinite DNG slabs pertaining to losses and source spectral characteristics, is conducted in Refs. [48,49] with the aid of time-dependent Green's functions. Its outcomes indicate that, for specific slab dimensions, the transient time can be effectively reduced by properly selecting the source's switching-on time. Consequently, it would indeed be very expedient for the design of a realistic lens system, if existing practices were enriched by accurate analytical relations between the temporal field evolution and the structure's geometrical and spectral traits.

It is the objective of this paper to develop a class of exact schemes for the time-domain electric field in infinite planar metamaterial slabs and examine the performance of their finite counterparts via optimized computational models. According to the principal aspects of this methodology, electric fields are expressed in terms of a double complex integral with respect to frequency and the longitudinal (parallel to slab faces) wave number component $k_{\parallel}$. In contast to previous approaches, which performed the integration through numerical means, a rigorous contour path technique for frequency-domain integration is incorporated to form analytical relations. In this context, a complete investigation, in the complex frequency plane, of the integrand poles coinciding with the surface polariton resonant frequencies is accomplished for different slab parameters. Successively, the

*tsibukis@auth.gr

frequency-domain integral, which concurs with the electric field generated by a current source of exponential longitudinal profile, is given as a compact sum of three purely analytical terms. Then, the integration of $k_{\|}$ is evaluated by a stationary phase approximation, expressing the total field as a superposition of two terms: one at the central frequency and the other at the surface polariton with zero group velocity. The analysis illustrates that, even in the absence of losses, unlike what has been formerly stated, transient phenomena tend to zero through an inverse square root law. In this way, the two contradictory occurrences, namely, the degenerated image quality of lossy configurations and the instabilities of lossless setups, during the design stage, are successfully circumvented. For the finite case, on the other hand, meticulous numerical simulations with an appropriately devised FDTD method display the presence of a highly resonant behavior, causing the excitation of several modes. Finally, a cavitylike approach is efficiently introduced to describe the overall phenomenon, and meaningful physical interpretations are carefully attempted. The results indicate an increase in the transient time, comparatively to the infinite slab, which is attributed to the confinement of resonant energy in the region of the DNG medium.

II. ANALYSIS OF INFINITE DNG SLABS: THEORETICAL FORMULATION

As already emphasized, a point of crucial importance in DNG superlensing systems is the derivation of an exact relation connecting the structure's geometric and electromagnetic parameters and the source's spectral features with the focusing efficiency and the transient phenomena damping time. This is essentially the aim of this section, where, through an enhanced mathematical algorithm, we derive a family of accurate analytical formulas for the temporal evolution of field quantities and the prompt calculation of amplitude and damping factors for the several surface modes. The key merit of our explicit criterion rests on the potential of directly choosing all structural parameters and so evade the conventional "trial and error" practices of most numerical methods, which entail successive and rather laborious simulations until the desired result is obtained. Hence, the total computational overhead is drastically diminished and the physical mechanisms that govern the slab's functional attributes receive an intuitive and sound interpretation.

Let us initiate our analysis by considering a lossy planar DNG slab, of width d along the x axis and infinite toward the y, z directions, as presented in Fig. 1. The metamaterial follows a dispersive Drude model for both ϵ_r and μ_r, with a plasma frequency ω_p and a collision factor Γ. The structure is illuminated by a current sheet $\mathcal{J}_s(y,z,t)$ on a constant x plane at distance d_s from the left-hand air-slab interface. For the sake of simplicity, the TE-polarized case is examined, i.e., the electric field intensity has only a z component. Then, only the z-directed part of the current source is nonzero and described by $\mathcal{J}_{sz}(y,t)=f(y)h(t)$, where $f(y)$ denotes the spatial distribution of the source and $h(t)$ its temporal evolution. Herein, we suppose that $h(t)=g_{on}(t)\sin(\omega_0 t)$, with $g_{on}(t)$ the modulation function expressing the transition from 0 (for $t<0$) to 1 (for $t\geqslant T$), T the transition time, and ω_0 the frequency at which the refractive index of the medium is $-1-j\gamma$. As will be proven later, a proper selection of $g_{on}(t)$ may yield smaller transient times for the image field.

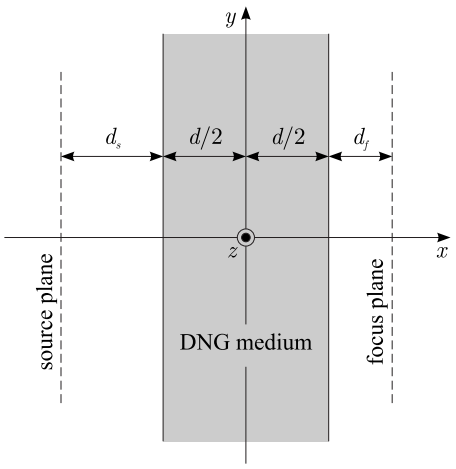

FIG. 1. Geometry of a planar DNG slab, infinite in the y, z directions, illuminated by a current source on a constant x plane.

A convenient means to express electric field intensity can be devised from the source spatial spectral content. In particular, $\mathcal{J}_{sz}(y,t)$ is represented as a superposition of the $J_{sz}(y,t;k_y)=e^{-jk_y y}h(t)$ currents, with $k_y\in\mathbb{R}$. In fact, the most significant terms are those with $|k_y|>\omega_0/c$, since they convey the subwavelength information of the source at ω_0 and each of them excites a unique set of surface plasmons, characterized via their $e^{-jk_y y}$ variation along the slab faces. This reestablishment of the initial general problem, amply serves our goal of developing analytical formulas for the field transient time, as the latter is fully determined by the surface plasmon temporal evolution. Thus, if $F(k_y)$ is the Fourier transform of $f(y)$ and $E_z(x,y,t;k_y)$ the field generated by $J_{sz}(y,t;k_y)$, the total field is described in terms of

$$\mathcal{E}_z(x,y,t)=\frac{1}{2\pi}\int_{-\infty}^{\infty}F(k_y)E_z(x,y,t;k_y)dk_y. \tag{1}$$

In turn, $E_z(x,y,t;k_y)$ is calculated by superimposing the effects of $H(\omega)e^{j(\omega t-k_y y)}$ currents, with $H(\omega)$ the temporal Fourier transform of $h(t)$. Eventually, at the focus plane $x=x_f$, one acquires

$$E_z(x_f,y,t;k_y)=-\frac{\mu_0 e^{-jk_y y}}{4\pi}\int_{-\infty}^{\infty}\frac{e^{j(\omega t-k_x d)}}{S(\omega)A(\omega)}H(\omega)\omega\, d\omega, \tag{2}$$

where

$$S(\omega)=k_x\cos\left(\frac{k_x' d}{2}\right)+j\frac{k_x'}{\mu_r}\sin\left(\frac{k_x' d}{2}\right), \tag{3a}$$

$$A(\omega)=\cos\left(\frac{k_x' d}{2}\right)+jk_x\frac{\mu_r}{k_x'}\sin\left(\frac{k_x' d}{2}\right), \tag{3b}$$

and $k_x=\sqrt{\omega^2/c^2-k_y^2}$, $k_x'=\sqrt{\mu_r\epsilon_r\omega^2/c^2-k_y^2}$ are the x-directed wave number components in the air and DNG slab, respec-

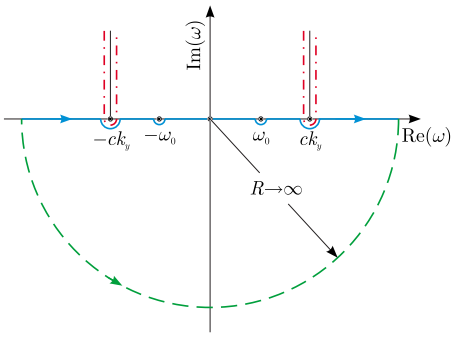

FIG. 2. (Color online) Integration paths for I in the complex ω plane.

tively, with $c=1/\sqrt{\mu_0\epsilon_0}$ the speed of light in vacuum. For clarity and throughout this paper, the integral in Eq. (2) is denoted as I, and its integrand as $K(\omega)$. Furthermore, the $S(\omega)$ and $A(\omega)$ terms correspond to the symmetrical and antisymmetrical surface modes, evolving at the air-metamaterial interfaces.

Since $K(\omega)$ is an even function with respect to k_x', the overall integration is not affected by the branches of k_x', in contrast to k_x, for which we should take into account its behavior in the complex ω plane. To this end, the latter is written as a product of two square roots, namely,

$$k_x = \frac{1}{c}\sqrt{\omega - ck_y}\sqrt{\omega + ck_y}. \tag{4}$$

Considering that the primary argument of z in $\sqrt{z}$ is restricted to the interval from $-\pi/2$ to $3\pi/2$, the branch cuts of k_x are the lines with $\mathrm{Re}(z)=\pm ck_y$ and $\mathrm{Im}(z)>0$. In fact, the presence of these branch cuts in the upper half ω plane, where $\mathrm{Im}(\omega)>0$, requires that the integration is conducted in the lower half plane, as depicted in Fig. 2 with the blue solid line. Moreover, and after some algebraic manipulations, it is found that the integral of $K(\omega)$ over the lower infinite semicircle (green dashed line in Fig. 2) is 0 for $t<(x_f-x_s)/c=2d/c$. This issue, together with the absence of poles in the lower complex semiplane, reveals that our choice for k_x satisfies the causality principle and therefore it is absolutely valid. The prior technique will be very enlightening in the derivation of the proposed analytical schemes as well as in the numerical calculation of I, intended to verify the accuracy and reliability of the methodology.

As illustrated in the ensuing formulation, the transient behavior of the DNG superlensing system is resolved by the surface plasmons whose oscillation frequencies lie near the central one. Since the plasmonic frequencies coincide with the poles of $K(\omega)$, it is instructive to stress some critical issues about them. The entire study is, again, limited for $|k_y|>\omega_0/c$, for the reasons exemplified in the previous paragraphs. First of all, we may attest that $H(\omega)$ has two poles at $\pm\omega_0$ for any finite $g_{on}(t)$ in the interval $[0,T]$, which provide the field pattern at the working frequency ω_0. Conversely, $S(\omega)$ and $A(\omega)$ are zeroed at an infinite number of ω_i^s and ω_i^a points in the right complex half plane, with index i receiving values from $-\infty$ to ∞. Because $S(\omega)$ and $A(\omega)$ are symmetrical with regard to the imaginary axis, the complex numbers $-(\omega_i^s)^*$ and $-(\omega_i^a)^*$ (the asterisk signifies the complex conjugate) are also their roots. Specifically, for $i=0$, the roots of $S(\omega)$ and $A(\omega)$ correspond to surface plasmons which decay exponentially in both the air and the DNG medium [38]. These roots have small imaginary parts for small losses, while their real parts are close to ω_0 and satisfy the $\mathrm{Re}(\omega_0^s)>\omega_0$, $\mathrm{Re}(\omega_0^a)<\omega_0$ relations. In this context, roots of negative i describe surface modes with an exponential decay in the air and a guided profile in the slab [39]. Their chief trait is that they involve small imaginary parts, as well. In contrast, $\omega_i^{s,a}$ of positive i tally with the lateral waves evolving at the air-metamaterial interfaces. The real and imaginary parts of these roots grow from 0 to ∞, as i increases. Figure 3 displays a graphical representation of $K(\omega)$ poles for a prescribed set of Drude parameters $\omega_p=\omega_0\sqrt{2}$, $\Gamma=5\times10^{-4}\omega_0$, and two different d.

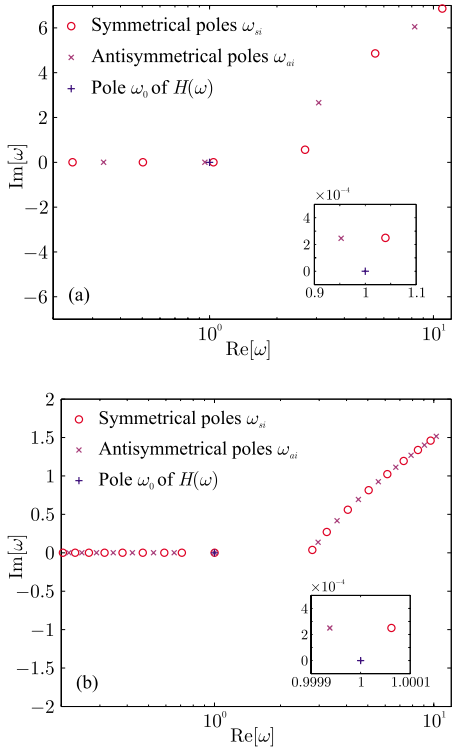

FIG. 3. (Color online) Poles of $K(\omega)$ in the $\mathrm{Re}(\omega)>0$ half plane for a DNG slab with a refractive index of $-1.0-j0.001$ at central frequency ω_0, $k_y=2.0k_0$, and $d=$(a) $0.2\lambda_0$, (b) $0.8\lambda_0$. The axes are normalized with respect to ω_0.

Having determined the appropriate theoretical assets, we next proceed to the development of the proposed approximate formula for I and, consequently, for $E_z(x_f,y,t;k_y)$, which is necessary for the extraction of the fields' transient behavior. If branch cuts were absent in the complex ω plane and since the integral of $K(\omega)$ along the upper infinite semicircle is zero for $t>T$, the residual theorem implies that I equals the sum of $K(\omega)$ residues at $\pm\omega_0$ and $\omega_i^{s,a}$, $-(\omega_i^{s,a})^*$. In the presence of branch cuts, however, their contribution to the computational procedure should be incorporated by any means, namely, the integrals of $K(\omega)$ around them (red dash-

dotted lines in Fig. 2). Also, due to the symmetry of $K(\omega)$, one may deduce that it is sufficient to calculate its integral—symbolized as I'—around the right-half-plane branch cut, or alternatively its integrals along the $\mathrm{Re}(\omega)=ck_y\pm\varepsilon$ and $\mathrm{Im}(\omega)>0$ lines, with ε an infinitesimal positive quantity. Another noteworthy remark is the considerably rapid reduction of the $e^{j\omega t}$ term in $K(\omega)$ for large t, as $\mathrm{Im}(\omega)$ increases from 0 to ∞ on the integration path of I'. This simply implies that, for large t values, $K(\omega)$ is nonzero solely for ω located very close to the real axis and I' is zero as a fairly acceptable and reliable approximation. Thus, I can be written as

$$I \cong j2\pi\left(\mathrm{Res}_{\omega_0}K + \mathrm{Res}_{-\omega_0}K + \sum_{i=-\infty}^{\infty}(\mathrm{Res}_{\omega_i^s}K + \mathrm{Res}_{\omega_i^a}K + \mathrm{Res}_{-(\omega_i^s)^*}K + \mathrm{Res}_{-(\omega_i^a)^*}K)\right), \tag{5}$$

where $\mathrm{Res}_{z_0}f$ denotes the residue of $f(z)$ at z_0. Additionally, because $H(\omega)$ decreases—at the worst case of $T=0$—according to an inverse square law away from ω_0, the only residues that essentially influence the computation of I are those at the $\omega_0^{s,a}$ and $-(\omega_0^{s,a})^*$ poles. So, bearing in mind that $K(\omega)$ is symmetrical on either side of the imaginary axis, Eq. (5) can be further simplified and, after some calculus, becomes

$$I \cong T_0 + T_0^s + T_0^a. \tag{6}$$

The term T_0 signifies temporal evolution at ω_0, while T_0^s and T_0^a correspond to the symmetrical and antisymmetrical surface plasmons, respectively. Their evaluation is precisely performed through

$$T_0 = 2\pi\omega_0\,\mathrm{Im}\left(\frac{e^{j[\omega_0 t - k_x(\omega_0)d]}}{S(\omega_0)A(\omega_0)}\right), \tag{7a}$$

$$T_0^s = -4\pi\,\mathrm{Im}\left(\frac{e^{j[\omega_0^s t - k_x(\omega_0^s)d]}}{S'(\omega_0^s)A(\omega_0^s)}H(\omega_0^s)\omega_0^s\right), \tag{7b}$$

$$T_0^a = -4\pi\,\mathrm{Im}\left(\frac{e^{j[\omega_0^a t - k_x(\omega_0^a)d]}}{S(\omega_0^a)A'(\omega_0^a)}H(\omega_0^a)\omega_0^a\right). \tag{7c}$$

Figure 4 depicts the absolute error in time between the approximate value of I, obtained from Eq. (6), and the exact one acquired via numerical integration for different k_y and d. Their evident agreement (very small errors) is indeed fairly promising, especially for large t, hence confirming the consistency of our conventions for Eq. (5).

Subsequently, our attention is concentrated on the estimation of the transient times for the infinite DNG slab through Eq. (6). With this objective, it is straightforward to detect that the main T_0 term, expressing the eligible part of the field, has a sinusoidal profile, namely, $T_0=A_0\sin(\omega_0 t+\varphi_0)$, with A_0 the amplitude and φ_0 the phase. In addition, the undesirable plasmonic $T_0^{s,a}$ quantities comply with the $T_0^{s,a}=A_0^{s,a}e^{-\mathrm{Im}(\omega_0^{s,a})t}\sin[\mathrm{Re}(\omega_0^{s,a})t+\varphi_0^{s,a}]$ relation, where $A_0^{s,a}$ and $\varphi_0^{s,a}$ denote the analogous amplitude and phase counterparts. Actually, these terms are responsible for various detrimental transient phenomena, which degrade the overall image quality. Notice that, in the lossless $[\mathrm{Im}(\omega_0^{s,a})=0]$ case, T_0^s and T_0^a never decay, leading the surface plasmon excitation to serious instabilities in the sense of the field's inability to reach a steadystate. Conversely, when losses are present, the transient terms follow an exponential decay rule with a damping coefficient of $\mathrm{Im}(\omega_0^{s,a})$. The above analysis is applicable for a sinusoidal current source along the y axis, like $f(y)=\sin(k_y y)$ or a DNG slab placed in a waveguide, where modes with such characteristics can be produced.

Nonetheless, the examination of an infinite slab, excited by an arbitrary source pattern, is definitely far more complicated. In particular, consistent with Eqs. (1) and (6), the total field is given by

$$\mathcal{E}_z(x_f,y,t) = -\frac{\mu_0}{8\pi^2}\int_{-\infty}^{\infty}F(k_y)T_0(k_y)e^{-jk_y y}dk_y - \frac{\mu_0}{8\pi^2}\int_{-\infty}^{\infty}F(k_y)T_0^s(k_y)e^{-jk_y y}dk_y - \frac{\mu_0}{8\pi^2}\int_{-\infty}^{\infty}F(k_y)T_0^a(k_y)e^{-jk_y y}dk_y. \tag{8}$$

The first integral in Eq. (8) provides the field distribution at the focus plane at central frequency ω_0 and is expressed as

$$\mathcal{E}_z^{\infty}(x_f,y,t) = -\frac{\omega_0\mu_0}{2\pi}A_{\infty}(y)\sin[\omega_0 t+\varphi_{\infty}(y)], \tag{9}$$

with $A_{\infty},\varphi_{\infty}$ satisfying the relation

$$A_{\infty}(y)e^{j\varphi_{\infty}(y)} = \int_0^{\infty}\mathrm{Re}[F(k_y)e^{-jk_y y}]\frac{e^{-jk_x(\omega_0)d}}{S(\omega_0)A(\omega_0)}dk_y. \tag{10}$$

On the other hand, the second and third integrals deal with the description of transient phenomena. Observing that $T_0^{s,a}(k_y)$ have the form of $a(k_y)e^{j\,\mathrm{Re}[\omega_0^{s,a}(k_y)]t}$, with $a(k_y)$ a smooth function of k_y, and employing a stationary phase approximation, it can be proven that, for large t values, the third integral is equal to zero and the second one is approximated through

$$\mathcal{E}_z^s(x_f,y,t) = \frac{\mu_0}{\pi}\,\mathrm{Re}[F(k_y^{st})e^{-jk_y^{st}y}]A_s^{st}\frac{e^{-\mathrm{Im}(\omega_{0,st}^s)t}}{\sqrt{t}} \times\sin[\mathrm{Re}(\omega_{0,st}^s)t+\varphi_s^{st}]. \tag{11}$$

The A_s^{st},φ_s^{st} terms satisfy the identity

$$A_s^{st}e^{j\varphi_s^{st}} = \frac{e^{-jk_x(\omega_{0,st}^s)d}}{S'(\omega_{0,st}^s)A(\omega_{0,st}^s)}H(\omega_{0,st}^s)\omega_{0,st}^s\sqrt{\frac{j2\pi}{\mathrm{Re}(\omega_0^s)''_{st}}}, \tag{12}$$

while k_y^{st} stands for the spatial frequency at which $d\omega_0^s/dk_y=0$. Furthermore, the subscript st in $\omega_{0,st}^s$ denotes that the specific quantity is computed at k_y^{st} and $\mathrm{Re}(\omega_0^s)''_{st}$ is the second derivative of $\mathrm{Re}(\omega_0^s)$ at k_y^{st} [for the detailed extraction of Eq. (8), see the Appendix].

It is important to stress that Eq. (11) is in agreement with the outcomes presented in Refs. [48,49], which attribute

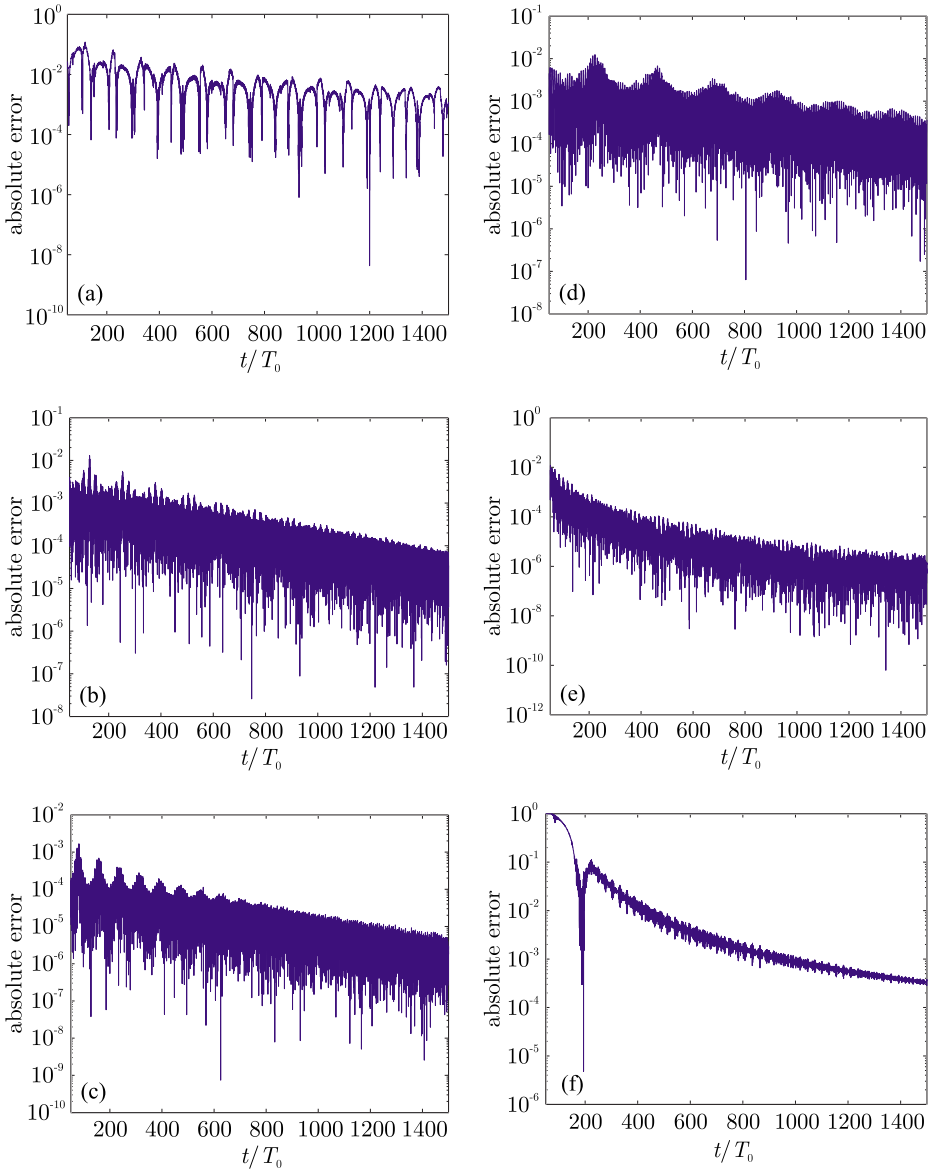

FIG. 4. (Color online) Absolute temporal error between approximate and exact I values for (a) $k_y=1.01k_0, d=0.2\lambda_0$, (b) $k_y=2k_0, d=0.2\lambda_0$, (c) $k_y=3k_0, d=0.2\lambda_0$, (d) $k_y=1.01k_0, d=0.8\lambda_0$, (e) $k_y=2k_0, d=0.8\lambda_0$, and (f) $k_y=3k_0, d=0.8\lambda_0$. The vertical axis is normalized with respect to ω_0/k_0.

$\mathcal{E}_z(x_f, y, t)$ fluctuations to the symmetrical surface polariton of zero group velocity $v_g=d\omega_0^s/dk_y$. According to the physical explanation, discussed in previous studies, this situation occurs because surface modes with $v_g \neq 0$ travel toward infinity away from $y=0$, counter to the mode with $v_g=0$, whose energy remains confined near the x axis, thus contributing to the field at the image plane. However, despite what has been previously reported, the $1/\sqrt{t}$ term in Eq. (11) implies that even in the lossless case the transient phenomena inside an infinite DNG slab decay very slowly and the field at the image plane attains a steady state. Such a significant conclusion is accredited to the participation of all surface polaritons, next to the one with $v_g=0$, in the evolution of $\mathcal{E}_z^s(x_f, y, t)$, as obtained from the stationary phase approximation. These polaritons possess nonzero, yet rather small, group velocity and propagate slowly toward infinity. Consequently, and as time elapses, unwanted oscillations are suppressed to zero, since the term with $v_g=0$ cannot exclusively achieve finite field amplitudes for source spatial distributions without a $\sin(k_y^{st}y)$ or $\cos(k_y^{st}y)$ quantity.

Typical forms of the electric field amplitude in the time domain, as acquired from Eqs. (9) and (11), are shown in Fig. 5 for a set of different γ and d. Clearly, as losses augment, the number of periods required for the system to reach steady state decreases. As far as d is concerned, amplitude oscillations in thinner slabs become considerable at larger frequencies, since $\omega_{0,st}^s$ deviates from ω_0 as d diminishes. Also, the propagation of electromagnetic waves through a thinner slab induces smaller attenuation losses, implying that A_∞ increases. Similar deductions can be drawn by the inspection of Fig. 6, which illustrates the amplitude ratio of the stationary surface polariton, E_{st}, to the main E_0 term at ω_0,

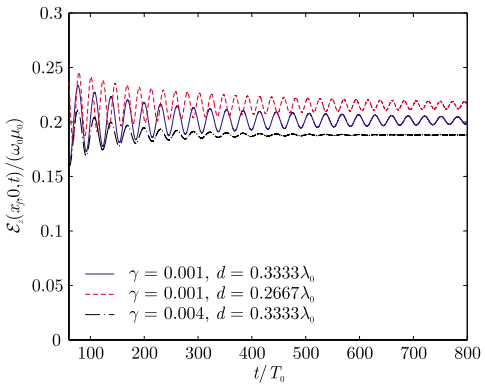

FIG. 5. (Color online) Temporal evolution of $\mathcal{E}_z(x_f,0,t)$ normalized to $\omega_0\mu_0$ for various γ and d.

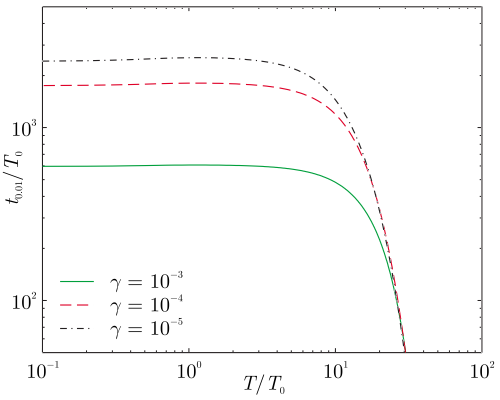

FIG. 7. (Color online) Variation of $t_{0.01}$ (damping time for $\kappa = 0.01$) versus the rise time T of $g_{on}(t)$ for $d=0.2\lambda_0$ and different γ.

obtained through a fast Fourier transform (FFT). The larger this ratio, the greater the contribution of the surface polariton. In addition, it becomes obvious that, except for its reduction with the growth of losses, the aforementioned ratio increases as the slab thickens, but with a constantly diminishing rate, until it reaches an upper bound. This phenomenon is ascribed to the fact that for large d the slab, regarding the surface modes, tends to adopt the behavior of a metamaterial half space, because the interaction between the slab interfaces, responsible for the generation of symmetrical and antisymmetrical modes, lessens.

It should be underlined, herein, that another advantage of our algorithm is the efficient derivation, via Eq. (11), of an exact relation among the transient time of the DNG superlensing structure and its geometrical parameters. Actually, if A_∞^0 is the steady-state amplitude at $y=0$, the time at which surface polaritons decay to κA_∞^0 is

$$t_\kappa = \frac{1}{2\ \mathrm{Im}(\omega_{0,st}^s)} r\left[\left(\frac{\omega_0 A_\infty^0}{2\ \mathrm{Re}[F(k_y^{st})]A_s^{st}}\right)^2 \frac{1}{2\ \mathrm{Im}[\omega_{0,st}^s]}\right], \tag{13}$$

where κ is a real number less than unity and $r(a)$ the root of the equation $e^{-x}=ax$. Note that, since $r(a)$ increases as a decreases and A_s^{st} is proportional to $H(\omega_{0,st}^s)$, larger T values result in smaller t_κ. In this framework, Fig. 7 presents the variation of $t_{0.01}$ with T for several γ, when the modulation function is

$$g_{on}(t) = \frac{1}{1+e^{-at}}, \tag{14}$$

with a a positive real constant. Even though $g_{on}(t)$ has not exactly the form described in the beginning of this section (not 0 for $t<0$ nor 1 for $t \geqslant T$), it is possible to choose T as the time needed for $g_{on}(t)$ to grow from 0.01 to 0.99. Examining the plots of Fig. 7, we observe that for small T, which means abrupt changes in the time domain or wide frequency content, t_κ is almost flat and strongly dependent on losses. As T increases, the spectral content of the initialization pulse at $\omega_{0,st}^s$ decreases and the symmetrical mode, accountable for amplitude fluctuations in the field, is not excited. The last deduction, in turn, leads to small transient times and independence of γ, which in Fig. 7 is depicted through the coincidence of the curves that correspond to different γ.

Finally, it is significant to stress that, although, the previous analysis deals with temporally dispersive and isotropic materials, it can be successfully extended to the more complicated, yet realistic, nonlocal, anisotropic media. Among them, wire media constitute an illustrative example. Structured in arrays, these substances (for wavelengths much larger than the inner period of the array) may be described by an effective plasmon-pole electric permittivity tensor [50]

$$\bar{\bar{\varepsilon}} = \varepsilon_0(\varepsilon_r \hat{\mathbf{x}}\hat{\mathbf{x}} + \hat{\mathbf{y}}\hat{\mathbf{y}} + \hat{\mathbf{z}}\hat{\mathbf{z}}), \quad \varepsilon_r(\omega,k_x) = 1 - \frac{\omega_p^2}{\omega^2 - c^2k_x^2}, \tag{15}$$

with the x axis parallel to the wires and ω_p the plasma frequency. Such media are broadly used in subwavelength imaging devices, either as a part of DNG lenses [51] or alone. The physical mechanism that governs the latter application is the potential of guiding electromagnetic waves along the wire medium axis with the speed of light and arbitrary transverse (perpendicular to the medium axis) wave number component [52]. In particular, the field at the back face of a slab, so devised, is given by an expression similar to Eq. (2); however, $S(\omega)$ and $A(\omega)$ are described via different relations.

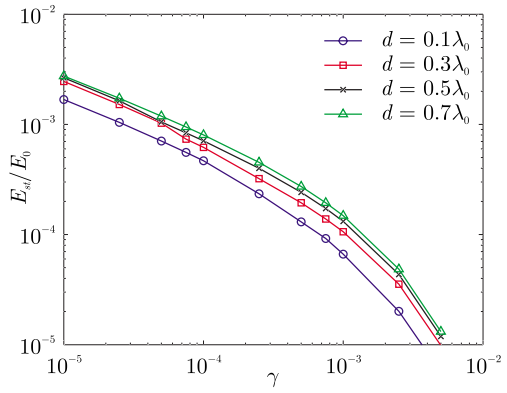

FIG. 6. (Color online) Amplitude ratio of the stationary E_{st} term to the main one E_0 as a function of γ for several d.

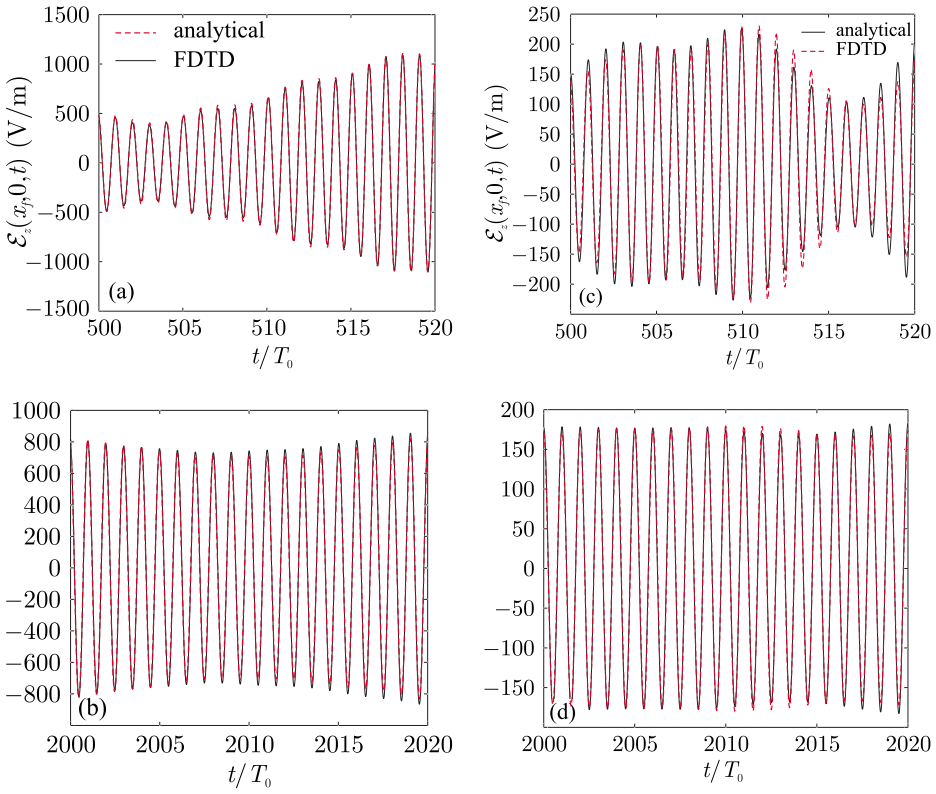

FIG. 8. (Color online) Theoretically and numerically extracted electric field values at two different time intervals for a DNG slab with $d=0.2\lambda_0$ and $k_y=$(a),(b) $1.01k_0$ and (c),(d) $1.5k_0$.

As already investigated, the roots of these new $S(\omega)$ and $A(\omega)$ provide the eigenfrequencies of specific eigenmodes traveling in the wire medium perpendicular to its axis. Since for specific k_y these roots are located on the real ω axis for zero losses, the excited eigenmodes oscillate constantly when the source has an exponential $e^{-jk_y y}$ profile parallel to the medium faces. Nevertheless, when a more realistic source, with a finite spatial distribution, is considered, the absence of any stationary points in the dispersion diagrams is estimated to result in the fast restoration of the steady state. This is in contrast with the local medium case, where the existence of a point with a zero group velocity in the symmetrical mode dispersion diagram imposes a slowly decaying transient phenomenon.

III. FINITE DNG SLAB MODELING: NUMERICAL RESULTS

After the successful extraction of these approximate schemes for the temporal evolution of electric fields at the image plane of an infinite planar DNG slab, the present section delves into the more realistic finite-slab case by means of a rigorous dispersive FDTD algorithm. Basically, the key motives for the implementation of the latter technique are the prohibitive difficulties arising in the development of pure time-dependent analytical solutions for the fields at these particular structures.

A critical issue for the consistent establishment of the FDTD method in DNG materials, where strong evanescent waves are involved, lies on the appropriate selection of its discretization spatial increment [46,53]. The impact of this observation is anticipated to be more intense in our simulations, whose duration lasts many periods, and even a small lattice reflection error is likely to produce serious and accumulating artificial discrepancies from the actual values. Therefore, before proceeding with the numerical results, it is deemed important to verify the accuracy of the frequency-dependent FDTD schemes in metamaterial applications, by comparing the variation of calculated and exact field components for a problem of known analytical solution. More specifically, consider an infinite planar slab illuminated by a source with a sinusoidal $\sin(k_y y)$ spatial profile, where the electric field at the image plane is given by Eq. (2). The slab is numerically manipulated via a parallel plate waveguide equivalent whose width is carefully chosen in order to allow the exclusive excitation of a certain evanescent mode [17]. The open ports of the structure are terminated by a complex frequency-shifted perfectly matched layer [54,55], suitably modified to cope with DNG media, while the current source is launched at a prefixed cross section of the waveguide. Figure 8 depicts the theoretically derived electric field compared to the numerically computed one, at two distinct temporal intervals, for a slab of $d=0.2\lambda_0$ and $k_y=1.01k_0$, $1.5k_0$. The spatial step of the method is set at $\Delta x=\Delta y=\lambda_0/100$. As deduced, the agreement between the results is very satisfactory, hence permitting us to reliably employ the proposed FDTD algorithm for the analysis of finite slabs.

Let us now assume the finite-sized counterpart of the planar DNG structure, depicted in Fig. 1, with a length L along the y axis. Figures 9(a) and 9(b) illustrate the temporal variation of the electric field amplitude at the $(x_f,0)$ image point before and after transient phenomena have damped down, for diverse L and $d=0.2\lambda_0$. Clearly, all steady-state outcomes

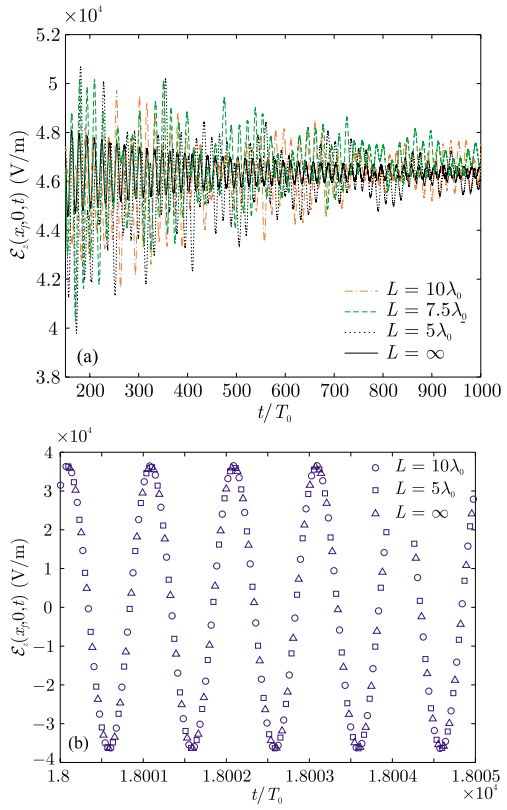

FIG. 9. (Color online) Electric field amplitude at $(x_f,0)$ image point for a DNG slab with a varying L and $d=0.2\lambda_0$ (a) before and (b) after the damping of transient phenomena.

obtained for both the finite and infinite slabs ($L=\infty$) are in excellent coincidence, confirming that the finite length does not drastically affect the behavior of the structure at the central frequency ω_0 [46]. Nevertheless referring to transient phenomena, substantial differences are observed. To be more specific, in contrast to the $L=\infty$ slab where only the $\omega^s_{0,st}$ surface plasmon contributes to the amplitude ripple, several modes are excited at the finite case. This phenomenon can be further exemplified by inspecting the FFT of the field, shown in Fig. 10. As derived, a dominant mode, which matches the highest peak of the spectrum, appears near the infinite-slab single mode, yet with a larger amplitude that keeps on escalating with the reduction of L. Also, secondary modes, whose

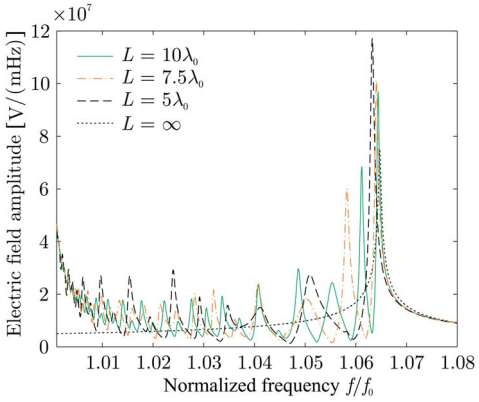

FIG. 10. (Color online) Frequency-domain electric field amplitude at $(x_f,0)$ image point for a DNG slab with a varying L and $d=0.2\lambda_0$.

population augments as the slab is elongated, arise between the central frequency and the dominant mode. It has to be mentioned that similar behavior is observed in the antisymmetric mode region, with the exception of smaller amplitudes and the absence of the dominant mode.

A possible explanation for the discrete number of surface modes can be provided by regarding a planar DNG slab as a waveguide, along the y direction, with modes the symmetric and antisymmetric surface plasmons. In this framework, the infinite slab corresponds to an unbounded waveguide, where surface modes travel freely toward infinity and contribute to the field image according to the mechanism described in the previous section. Conversely, in a finite slab, surface plasmons are reflected at its edges, with the whole structure acting like a resonator which allows the generation of specific modes. Figure 11 presents the spatial profile of field amplitude for the first six modes (the dominant one included), while $L=10\lambda_0$ and $d=0.2\lambda_0$. In all cases, the field is confined in the $-L/2\leqslant y\leqslant L/2$ span, thus proving the claim that the finite length leads to a resonatorlike performance. Moreover, the amplitude maxima and zeros point out the presence of stationary waves, as occurs in a real resonator. The fluctuations in the maximum amplitude are attributed to the existence (in pairs) of surface plasmons, with different transverse wave numbers for frequencies between ω_0 and $\omega^s_{0,st}$, due to the form of the dispersion relation $S(\omega;k_y)=0$. On the other

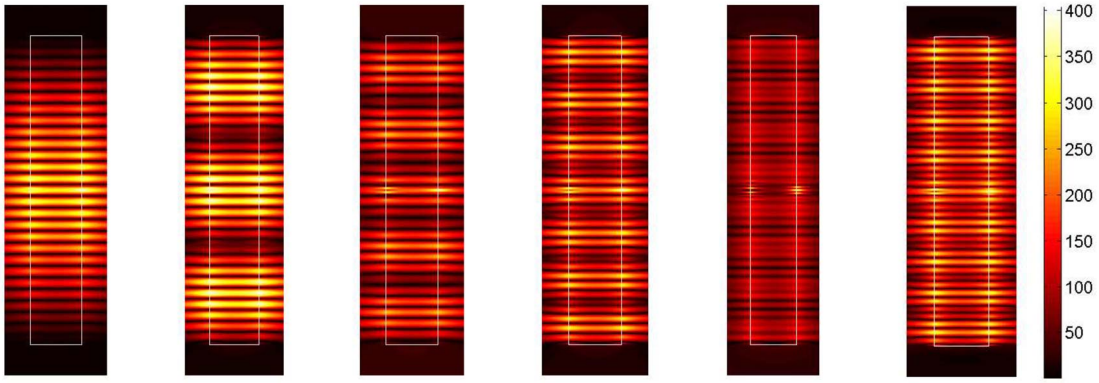

FIG. 11. (Color online) Spatial profile of the electric field for the first six modes of a planar DNG slab with $L=10\lambda_0$ and $d=0.2\lambda_0$.

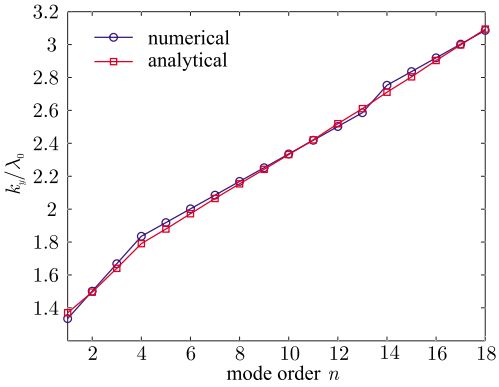

FIG. 12. (Color online) Variation of k_y versus mode order n, numerically calculated, via a spatial FFT, and analytically acquired, through the dispersion relation.

hand, Fig. 12 describes k_y for each surface mode of a slab with $L=10\lambda_0$ and $d=0.2\lambda_0$, obtained numerically via a spatial FFT and analytically through the previous dispersion relation. The promising coincidence between the results validates our initial supposition that surface plasmons in a finite slab play the role of resonant modes in a cavity.

An alternative and equally instructive interpretation of the cavity effect may be accomplished through Fig. 13, which shows the k_y variation as a function of mode order for different L and d. By the term "mode order," we presume an integer n exclusively referring to a specific mode, with 1 the value for the dominant one. Note that, in ordinary rectangular or circular cavities, n is related to the phase constant k_y of each mode via $k_yL=n\pi$ and expresses the number of field nullifications along the cavity length L. So k_y is proven to be proportional to n with the modes forming a line of slope π/L in the k_y-n plane. A similar behavior is detected for the planar finite DNG slab, as well. In particular, Fig. 13 verifies that the dependence of k_y and n is linear, aside from a slight deviation for small n. Since the excitation source is placed on the y axis, which coincides with the structure's center along the x direction, we have to consider only those surface modes with a nonzero amplitude at $x=0$. This situation, in the usual cavities, is equivalent to taking into account the modes for which n is an odd number or $k_yL=(2m+1)\pi$. Differently speaking, the slope of the finite slab k_y-n lines is expected to be around $2\pi/L$. In Table I, one can observe the numerically and theoretically extracted slopes of the curves plotted in Fig. 13. Their considerable agreement, especially for $d=0.2\lambda_0$ and large L choices, substantiates, again, the consistency of our conclusion that a finite DNG slab behaves like a resonant cavity.

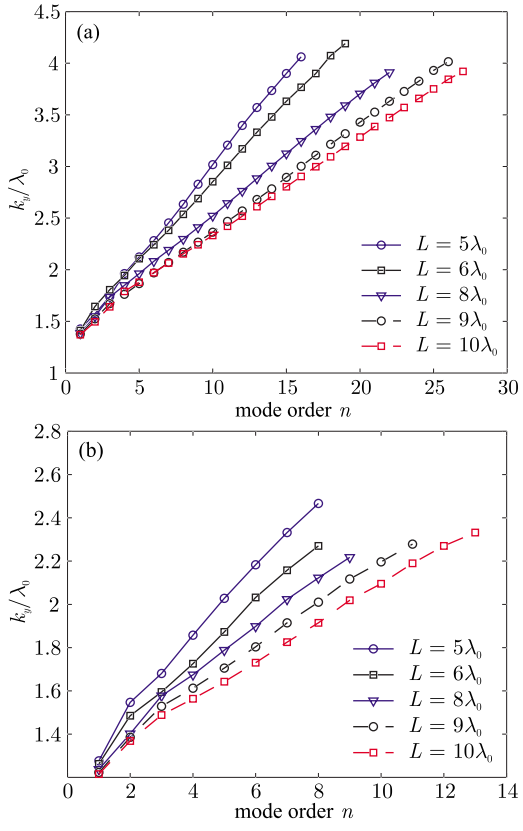

FIG. 13. (Color online) Variation of k_y versus mode order n, for different L and $d=$(a) $0.2\lambda_0$ and (b) $0.4\lambda_0$.

TABLE I. Numerically calculated and theoretically predicted slope values of the curves in Fig. 13, for planar DNG slabs with $d=0.2\lambda_0$ and $0.4\lambda_0$ and diverse L.

L	$d=0.2\lambda_0$	$d=0.4\lambda_0$	Theoretical
$5\lambda_0$	0.1788	0.1658	0.2
$6\lambda_0$	0.1527	0.1414	0.1667
$8\lambda_0$	0.1180	0.12	0.125
$9\lambda_0$	0.1043	0.1026	0.1111
$10\lambda_0$	0.0959	0.0909	0.1

Nonetheless, the linearity deviations appearing in Fig. 13 for modes near the dominant one constitute an issue of further investigation. A rational explanation for this result rests on the fact that, due to the dispersion relation, at each resonant frequency there exist two surface polaritons, for instance α and β, with distinct transverse wave numbers $k_y^\alpha < k_y^{st}$ and $k_y^\beta > k_y^{st}$, respectively. If the amplitudes of these modes are A_α and A_β, the electric field boundary condition at slab edges is, approximately, $A_\alpha \sin(k_y^\alpha L/2)+A_\beta \sin(k_y^\beta L/2)=c$, with c a small real number accounting for the lack of edges to act as perfect electric or magnetic walls. Also, notice that both sinusoidal terms stem from the practically complete reflection of surface modes at $x=\pm L/2$. For resonant frequencies near ω_0, simulations show that A_α is much smaller than A_β ($A_\beta/A_\alpha \sim 10$), which simplifies the boundary condition to $A_\beta \sin(k_y^\beta L/2)=c$, with solutions given by $k_yL=2m\pi+\sin^{-1}c$, for $m \in \mathbb{N}$. Even though the last equation does not explicitly involve n, consecutive m generate successive modes, permitting the derivation of a linear relation between m and n, that, in turn, indicates the linear dependence of k_y on n. In contrast, as one reaches the stationary symmetrical surface mode, A_α becomes comparable to A_β and the solution of the boundary condition is nonlinear with respect to n.

As already introduced in the previous section, a decisive factor that characterizes the slab's behavior is the transient

TABLE II. Transient time $t_{0.01}$ normalized to T_0 for planar DNG slabs with $d=0.2\lambda_0$ and $0.4\lambda_0$ and diverse L, including the infinite case.

L	$d=0.2\lambda_0$	$d=0.4\lambda_0$
$5\lambda_0$	1.2974×10^3	1.3674×10^3
$6\lambda_0$	1.7116×10^3	1.5101×10^3
$7\lambda_0$	1.2101×10^3	1.2177×10^3
$8\lambda_0$	1.4422×10^3	1.5747×10^3
$9\lambda_0$	1.4159×10^3	1.4276×10^3
$10\lambda_0$	1.5291×10^3	1.4621×10^3
∞	596.21	753.82

phenomena damping time t_κ. Table II provides $t_{0.01}$ for slabs with varying dimensions and $\gamma=0.001$, along with the corresponding value for an infinite slab of the same d. A first deduction is that $t_{0.01}$ of the finite slab is about three times larger for $d=0.2\lambda_0$ and two times larger for $d=0.4\lambda_0$ than its infinite slab counterpart. This difference is in absolute agreement with the resonatorlike description, since the excited modes in the finite slab obtain greater amplitudes than those in the infinite structure, due to the energy confinement in the metamaterial region. Actually, it is the totally different mechanism of mode excitation between the two cases that justifies such discrepancies. To be more exact, in the infinite slab the almost zero group velocity results in very slow mode propagation near $\omega^s_{0,st}$ toward infinity and creates a certain amplitude fluctuation. In the finite case, on the other hand, the excited modes oscillate inside the slab edges, irrespective of their group velocity, and the only way they can be damped down is through losses. The last remark is clearly confirmed by means of Fig. 14 which displays the transient phenomena amplitude for a lossless slab with $L=7\lambda_0$ and $d=0.2\lambda_0$ compared to its infinite analogue. Note that the amplitude in the finite slab is always larger than that of the infinite case. Lastly, in the former structures, surface modes do not attenuate as occurs in the latter (according to a $1/\sqrt{t}$ law), with the exception of small temporal intervals.

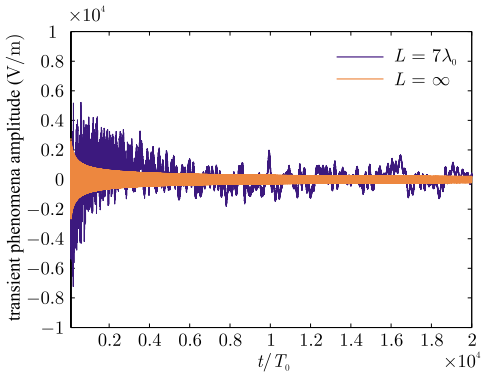

FIG. 14. (Color online) Transient phenomena temporal evolution for a planar DNG slab with $L=7\lambda_0$ compared with the corresponding infinite one, when $d=0.2\lambda_0$ and $\gamma=0$.

IV. CONCLUSION

In this paper, the transient behavior of arbitrarily sized planar DNG slabs has been elaborately explored, from both analytical and numerical points of view, in terms of an integrated methodology. In particular, an exact formula for the temporal evolution of the field, when the source is sinusoidally distributed along the longitudinal direction, has been derived through a complete contour path integration. Apart from the main term of interest at frequency ω_0, where $\epsilon_r=\mu_r=-1-j\gamma$, a symmetric and an antisymmetric surface polariton are excited at adjacent frequencies, whose amplitudes decrease with time according to an exponential rule that depends on losses. In the lossless case, however, the transient phenomena are never damped down and the image is unstable. Furthermore, a relation for the time-domain field induced by an arbitrary source has been developed, exhibiting an exponential and an inverse square root decrease of the excited stationary polariton amplitude with time. In contrast to the sinusoidal source, the presence of the square root term imposes a very slow attenuation on the transient amplitude, which has not been predicted by previous works. Equivalently, the transient time, which can now be readily computed without the need of any laborious numerical simulation, has been proven to be directly associated with the source spectral content at the resonant frequency.

Moreover, the proposed analysis examined the finite DNG slab case via a precise dispersive FDTD algorithm. The results indicate substantial amplitude fluctuations, larger than those of infinite structures, which after a temporal and spatial FFT were interpreted through a cavitylike effect. In this context, each cavity mode coincides with a specific surface polariton, while its phase constant follows a linear relation with respect to mode order, as happens in regular cavities. A slight nonlinearity arising for small orders is attributed to the excitation of a couple of surface polaritons at a single frequency, owing to the dispersion relation. This highly resonant behavior of finite slabs yields greater transient times, especially for the lossless case. Extensive investigations have also revealed that the transient time is, primarily, determined by the dominant surface mode, located near the stationary counterpart. Finally, among potential future perspectives is the derivation of analytical formulas for the excited modes of finite metamaterial slabs, similar to the ones for the infinite case.

ACKNOWLEDGMENTS

This work has been supported by the Greek General Secretariat of Research and Technology under Grant No. PENED03/03ED936.

APPENDIX: DERIVATION OF Eq. (11)

In this appendix, we provide the calculation process for the second term (ST) on the right-hand side of Eq. (8). Observing Eq. (8), the ST is extracted by integration from $-\infty$ to ∞ with respect to k_y, which involves $F(k_y)$ and $T_0^s(k_y)$ as well. Because $f(y)$ is a real function of y, it entails that $F(-k_y)=F^*(k_y)$. Furthermore, ω_0^s is an even function of k_y, resulting

in $T_0^s(-k_y)=T_0^s(k_y)$. Therefore, bearing in mind Eq. (7), the ST can be expressed as

$$\frac{\mu_0}{\pi}\,\mathrm{Im}\left(\int_0^\infty \frac{e^{j[\omega_0^s t-k_x(\omega_0^s)d]}}{S'(\omega_0^s)A(\omega_0^s)}H(\omega_0^s)\omega_0^s \mathrm{Re}[F(k_y)e^{-jk_y y}]dk_y\right). \tag{A1}$$

The previous integral can be computed for large t by means of the stationary phase approximation, which states that for large λ values the definite integral

$$I=\int_a^b f(x)e^{j\lambda g(x)}dx \tag{A2}$$

of smooth functions $f(x)$ and $g(x)$, with $g(x)$ real, is approximated by

$$I \simeq f(c)e^{j\lambda g(c)}\sqrt{\frac{j2\pi}{\lambda g''(c)}}, \tag{A3}$$

for c the stationary point of $g(x)$ in the $[a,b]$ span. Herein, $x\equiv k_y$, $\lambda\equiv t$, $g(x)\equiv \mathrm{Re}[\omega_0^s(k_y)]$,

$$f(x)\equiv \mathrm{Re}[F(k_y)e^{-jk_y y}]\frac{e^{-\mathrm{Im}(\omega_0^s)t}e^{-jk_x(\omega_0^s d)}}{S'(\omega_0^s)A(\omega_0^s)}H(\omega_0^s)\omega_0^s,$$

and $c=k_y^{st}$ is the longitudinal wave number at which $d\omega_0^s/dk_y=0$. Consequently, if $\omega_{0,st}^s$ is the symmetrical surface polariton frequency at k_y^{st}, the ST is obtained via

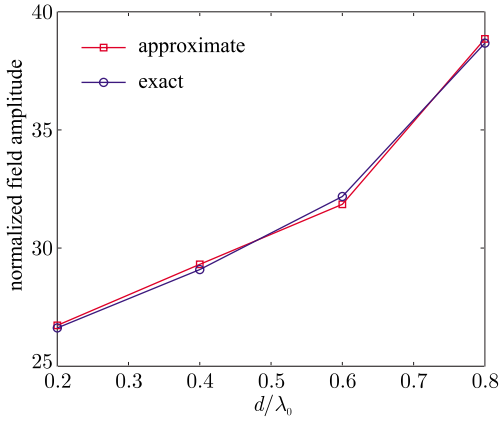

FIG. 15. (Color online) Electric field amplitude at $\omega_{0,st}^s$ acquired through the numerical calculation of Eq. (A1) (exact) and the approximate formula of Eq. (A4), for different d (y axis is normalized to $\omega_0\mu_0$).

$$(\mathrm{ST})=\frac{\mu_0}{\pi}\,\mathrm{Im}\left([F(k_y^{st})e^{j[\omega_{0,st}^s t-k_y^{st}y]}]\frac{e^{-jk_x(\omega_{0,st}^s d)}}{S'(\omega_{0,st}^s)A(\omega_{0,st}^s)}\times H(\omega_{0,st}^s)\omega_{0,st}^s\sqrt{\frac{j2\pi}{t\,\mathrm{Re}(\omega_{0,st}^s)''}}\right), \tag{A4}$$

which is equivalent to Eqs. (11) and (12). An indication of the validity of Eq. (A4) can be seen in Fig. 15, which depicts the FFT electric field amplitude at $\omega_{0,st}^s$, as evaluated by the numerical integration of Eq. (A1) and the proposed approximate expression of Eq. (A4).

[1] V. G. Veselago, Sov. Phys. Usp. **47**, 509 (1968).
[2] J. B. Pendry, A. J. Holden, W. J. Stewart, and I. Youngs, Phys. Rev. Lett. **76**, 4773 (1996).
[3] J. B. Pendry, A. J. Holden, D. J. Robbins, and W. J. Stewart, IEEE Trans. Microwave Theory Tech. **47**, 2075 (1999).
[4] R. Marqués, F. Mesa, J. Martel, and F. Medina, IEEE Trans. Antennas Propag. **51**, 2572 (2003).
[5] C. L. Holloway, E. F. Kuester, J. Baker-Jarvis, and P. Kabos, IEEE Trans. Antennas Propag. **51**, 2596 (2003).
[6] C. R. Simovski and S. He, Phys. Lett. A **311**, 254 (2003).
[7] H. Chen, L. Ran, J. Huangfu, X. Zhang, K. Chen, T. M. Grzegorczyk, and J. A. Kong, Phys. Rev. E **70**, 057605 (2004).
[8] A. Grbic and G. V. Eleftheriades, IEEE Trans. Antennas Propag. **51**, 2604 (2003).
[9] C. Caloz and T. Itoh, IEEE Microw. Wirel. Compon. Lett. **13**, 547 (2003).
[10] P. P. M. So, H. Du, and W. J. R. Hoefer, IEEE Trans. Microwave Theory Tech. **53**, 1496 (2005).
[11] D. R. Smith, W. J. Padilla, D. C. Vier, S. C. Nemat-Nasser, and S. Schultz, Phys. Rev. Lett. **84**, 4184 (2000).
[12] C. Caloz and T. Itoh, *Electromagnetic Metamaterials: Transmission Line Theory and Microwave Applications. The Engineering Approach* (John Wiley & Sons, New York, 2006).
[13] N. Engheta and R. W. Ziolkowski, *Electromagnetic Metamaterials: Physics and Engineering Explorations* (John Wiley & Sons, New York, 2006).
[14] S. A. Cummer, Appl. Phys. Lett. **82**, 1503 (2003).
[15] X. S. Rao and C. K. Ong, Phys. Rev. B **68**, 113103 (2003).
[16] X. S. Rao and C. K. Ong, Phys. Rev. E **68**, 067601 (2003).
[17] M. W. Feise, J. B. Schneider, and P. J. Bevelacqua, IEEE Trans. Antennas Propag. **52**, 2955 (2004).
[18] A. N. Lagarkov and V. N. Kissel, Phys. Rev. Lett. **92**, 077401 (2004).
[19] A. Grbic and G. V. Eleftheriades, Phys. Rev. Lett. **92**, 117403 (2004).
[20] S. Maslovski, S. Tretyakov, and P. Alitalo, J. Appl. Phys. **96**, 1293 (2004).
[21] E. A. Semouchkina, G. B. Semouchkin, M. Lanagan, and C. A. Randall, IEEE Trans. Microwave Theory Tech. **53**, 1477 (2005).
[22] J. D. Baena, L. Jelinek, R. Marqués, and F. Medina, Phys. Rev. B **72**, 075116 (2005).
[23] F. Mesa, M. J. Freire, R. Marqués, and J. D. Baena, Phys. Rev. B **72**, 235117 (2005).
[24] A. A. Sukhorukov, I. V. Shadrivov, and Y. S. Kivsar, Int. J. Numer. Model. **19**, 105 (2006).
[25] D. L. Sounas, N. V. Kantartzis, and T. D. Tsiboukis, IEEE Trans. Microwave Theory Tech. **54**, 4111 (2006).

[26] K. G. Balmain, A. E. Lüttgen, and P. Kremer, IEEE Antennas Wireless Propag. Lett. **1**, 146 (2002).
[27] A. Alù and N. Engheta, IEEE Trans. Antennas Propag. **51**, 2558 (2003).
[28] E. Ozbay, K. Aydin, E. Cubukcu, and M. Bayindir, IEEE Trans. Antennas Propag. **51**, 2592 (2003).
[29] R. W. Ziolkowski and A. D. Kipple, IEEE Trans. Antennas Propag. **51**, 2626 (2003).
[30] I. A. Eshrah, A. A. Kishk, A. B. Yakovlev, and A. W. Glisson, IEEE Trans. Microwave Theory Tech. **53**, 3298 (2005).
[31] P. Baccarelli, P. Burghignoli, F. Frezza, A. Galli, P. Lampariello, G. Lovat, and S. Paulotto, IEEE Trans. Microwave Theory Tech. **53**, 32 (2005).
[32] M. Gil, J. Bonache, I. Gil, J. García-García, and F. Martín, Int. J. Numer. Model. **19**, 87 (2006).
[33] A. Alù, F. Bilotti, N. Engheta, and L. Vegni, IEEE Trans. Antennas Propag. **55**, 1698 (2007).
[34] N. V. Kantartzis, D. L. Sounas, C. S. Antonopoulos, and T. D. Tsiboukis, IEEE Trans. Magn. **43**, 1329 (2007).
[35] N. Katsarakis, I. Tsiapa, A. Kostopoulos, G. Konstantinidis, R. S. Penciu, T. F. Gundogdu, M. Kafesaki, E. N. Economou, T. Koschny, and C. M. Soukoulis, Appl. Phys. Lett. **89**, 084103 (2006).
[36] J. B. Pendry, Phys. Rev. Lett. **85**, 3966 (2000).
[37] R. Ruppin, Phys. Lett. A **277**, 61 (2000).
[38] R. Ruppin, J. Phys.: Condens. Matter **13**, 1811 (2001).
[39] B. Wu, T. M. Grzegorczyk, Y. Zhang, and J. A. Kong, J. Appl. Phys. **93**, 9386 (2003).
[40] A. Ishimaru, J. R. Thomas, and S. Jaruwatanadilok, IEEE Trans. Antennas Propag. **53**, 915 (2005).
[41] D. R. Smith, D. Schurig, M. Rosenbluth, S. Schultz, S. A. Ramakrishna, and J. B. Pendry, Appl. Phys. Lett. **82**, 1506 (2003).
[42] L. Lu, Y. Hao, and C. G. Parini, IEE Proc.: Sci., Meas. Technol. **151**, 403 (2004).
[43] T. J. Cui, Z.-C. Hao, X. X. Yin, W. Hong, and J. A. Kong, Phys. Lett. A **323**, 484 (2004).
[44] L. Chen, S. He, and L. Shen, Phys. Rev. Lett. **92**, 107404 (2004).
[45] J. J. Chen, T. M. Grzegorczyk, B. I. Wu, and J. A. Kong, Opt. Express **13**, 10840 (2005).
[46] Y. Zhao, P. Belov, and Y. Hao, Phys. Rev. E **75**, 037602 (2007).
[47] G. Gomez-Santos, Phys. Rev. Lett. **90**, 077401 (2003).
[48] L. Zhou and C. T. Chan, Appl. Phys. Lett. **86**, 101104 (2005).
[49] X. Huang, L. Zhou, and C. T. Chan, Phys. Rev. B **74**, 045123 (2006).
[50] P. A. Belov, R. Marqués, S. I. Maslovski, I. S. Nefedov, M. Silveirinha, C. R. Simovski, and S. A. Tretyakov, Phys. Rev. B **67**, 113103 (2003).
[51] P. Ikonen, M. Lapine, I. Nefedov, and S. Tretyakov, Prog. Electromagn. Res. **63**, 279 (2006).
[52] P. A. Belov and M. G. Silveirinha, Phys. Rev. E **73**, 056607 (2006).
[53] A. Taflove and S. C. Hagness, *Computational Electrodynamics: The Finite-Difference Time-Domain Method* (Artech House, Norwood, MA, 2005).
[54] J. A. Roden and S. D. Gedney, Microwave Opt. Technol. Lett. **27**, 334 (2000).
[55] J.-P. Bérenger, IEEE Microw. Wirel. Compon. Lett. **12**, 218 (2002).